



Modelling the keyhole profile in laser welding through energy balance including the local contribution of multiple reflections through the plasma by ray tracing

Donato Coviello^{a,b}, Antonio D'Angola^{b,c}, Donato Sorgente^{d,*}, Alexander F.H. Kaplan^e

^a Baosteel Tailored Blanks Srl, PZ, Tito Scalo, Italy

^b Department of Engineering, Università degli Studi della Basilicata, Potenza, Italy

^c Institute for Plasma Science and Technology, CNR ISTP Bari Section, Bari, Italy

^d Department of Mechanics, Mathematics and Management, Politecnico di Bari, Bari, Italy

^e Department of Engineering Sciences and Mathematics, Luleå University of Technology, Luleå, Sweden

ARTICLE INFO

Keywords:

Laser
Welding
Keyhole
Ray-tracing
Energy balance
Plasma absorption

ABSTRACT

Several numerical and analytical methods were developed over the years in the attempt to properly model the keyhole laser welding. Among them, semi-analytical models revealed to be effective and efficient for the calculation of the keyhole geometry. They can take into account the plasma absorption mechanism through inverse Bremsstrahlung, as well as the effects related to the multiple reflection phenomena that the laser beam rays experience in the keyhole cavity, with relatively low computational costs. However, multiple reflections contribution was usually calculated through a very simple average estimation. In this work, a semi-analytical model that employs an iterative ray-tracing technique for the calculation of multiple reflections inside the keyhole is described. The approach can take precisely into account the absorption mechanism for each laser beam ray along its segmented path in the keyhole considering also the commonly neglected-upward oriented reflections. The energy transferred to the molten material due to all the rays hitting the keyhole wall is locally considered for the energy balance and the keyhole is recalculated iteratively until the profile does not significantly deviate from the previous one. The laser beam attenuation due to the plasma plume that develops above the keyhole is also considered, for a CO₂-laser, investigating different plume height values. A numerical-experimental comparison considering two different laser welding setups is then performed. The results show that both the upward-oriented reflections and the plasma plume damping have noticeable effects on the cavity shape and depth, while the numerical-experimental comparison reveals that the model is able to predict keyhole depths, especially for welding configurations with higher heat input values.

1. Introduction

Nowadays laser welding, and in particular keyhole welding, is a well-established and commonly used metal joining technique in the automotive and aerospace fields. Unlike other conventional heat sources, with which the metal is simply heated up until melting, the laser beam source is able to supply very high power densities that allow the formation of the keyhole according to the power density ($\geq 10^9$ W/m² according to [1,2]; $\geq 10^{10}$ W/m² according to [3–5]), its intensity distribution and the material thermo-physical properties [6]. This lets the material reach temperatures higher than its boiling point forming intensive metal evaporation above the ambient pressure, which causes a

reactive force in terms of vapor pressure, named recoil pressure or ablation pressure, that accelerates the melt in a complex manner, causing a wavy surface, forming the keyhole cavity [1,3]. Therefore, the keyhole turns out to be a long and very narrow channel that follows the movements of the laser beam. For this reason, keyhole laser welded seams are characterized by high aspect ratios and small heat-affected zones. Laser keyhole welding is a complex process since it involves several physical phenomena, such as light-matter interaction, heat conduction, melting, vaporization, plasma generation, fluid flow, and surface deformation. Many attempts of direct keyhole observation were done trying to better understand this process, even if some aspects continue to be unclear due to the difficulties related to the direct

* Corresponding author.

E-mail address: donato.sorgente@poliba.it (D. Sorgente).

<https://doi.org/10.1016/j.jmapro.2025.06.032>

Received 22 November 2024; Received in revised form 24 April 2025; Accepted 7 June 2025

Available online 16 June 2025

1526-6125/© 2025 The Authors. Published by Elsevier Ltd on behalf of The Society of Manufacturing Engineers. This is an open access article under the CC BY license (<http://creativecommons.org/licenses/by/4.0/>).

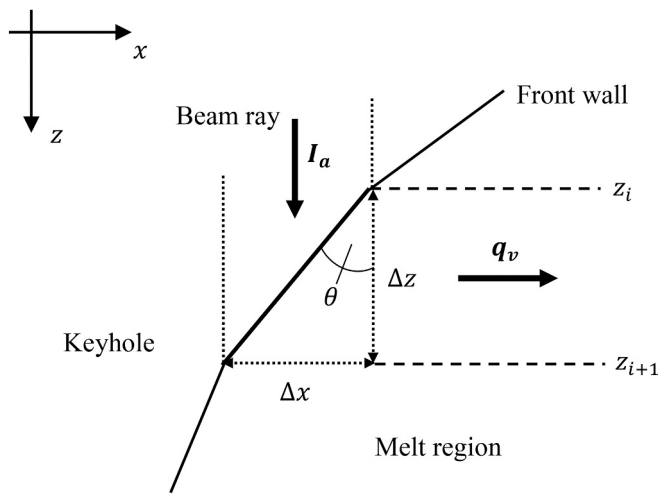


Fig. 1. Schematization of the energy balance on a generic cell of the model on the front wall.

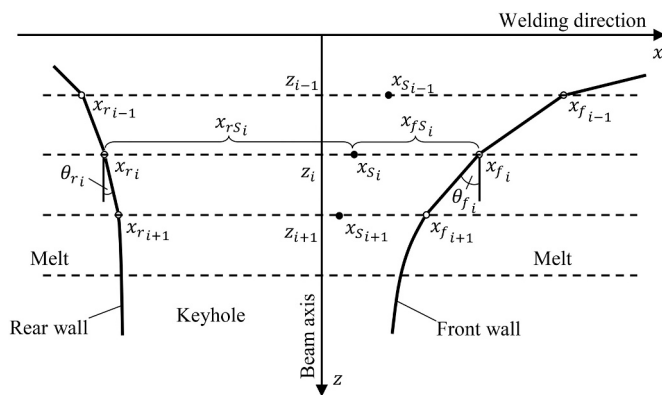


Fig. 2. Schematization of the point-by-point calculation of the keyhole profile (adapted from [22]).

observation of these phenomena [7–15]. Among the experimental techniques adopted, high-speed imaging allows observation limited only to the surface of the melt pool and the plasma plume, while X-ray techniques let a deeper investigation of the dynamic phenomena into the keyhole and the molten pool. In any case, experimental observations usually require complicated and expensive equipment, and not always are able to investigate the keyhole dynamics in detail. Therefore, several numerical and analytical models were created to include all the physical phenomena involved in the process [16–19]. Among them, semi-analytical approaches are effective and relatively low-computational-cost methods for the prediction of the keyhole geometry. Semi-analytical models continue to play an important role in understanding physical phenomena that are not yet fully clarified. They can provide sufficiently accurate estimations while requiring significantly less computational effort than more accurate model [20,21]. In addition, the results obtained can be implemented in more complex CFD simulations to better capture the whole phenomena involved. The most innovative semi-analytical approaches are able to take into account the energy, pressure, and velocity balance at the liquid-vapor interface (i.e., the keyhole wall) through a point-by-point in-depth calculation, as well as the effect of high welding speeds, which entails an asymmetrical keyhole profile, adopting different balance calculations for the front keyhole wall (i.e. the half of the liquid-vapor interface which precedes the laser beam) and the rear one (i.e. the other half which follows the laser beam) [22–30]. These approaches can consider also the effects related to the laser beam damping in the plasma generated inside and over the keyhole

and the multiple reflection phenomena of the laser beam that occur inside the cavity. For CO₂-laser beams the plasma absorption coefficient is about two orders of magnitude stronger (quadratic to the wavelength) than for near infrared (NIR) lasers, like fibre lasers. For NIR lasers, any plasma interaction remains usually weak, but vapor scattering can significantly alter the propagation of the focused laser beam, often in a fluctuating manner, affecting in turn the keyhole. Several authors considered multiple reflections by ray tracing during sophisticated CFD-simulation of the melt pool and keyhole [31–33] and demonstrated how multiple reflection phenomena are strongly related to the keyhole geometry [34]. However very seldom some explicit analysis of the multiple reflection behaviour of rays was published. Some authors [35,36] measured the remaining power reflected back from the keyhole, as a relation to the total absorption. In particular, those authors conducted experiments in which the keyhole shape was acquired via in-situ X-ray imaging, and the reflected laser energy was measured using an integrating sphere. The absorbed energy was then deduced by subtracting the reflected portion from the total incident energy. To interpret these measurements, ray-tracing models were used based on simplified geometries observed experimentally. Importantly, in these studies, the angular distribution of reflected rays, particularly those exiting the keyhole in the upward direction, is a key parameter in understanding how the energy is coupled to the material. Although these ray-tracing models do not explicitly include absorption via inverse Bremsstrahlung, the significance of upward-reflected rays is implied by their impact on the experimentally measured energy losses. In a previous work [37], a semi-analytical model for the calculation of an asymmetrical keyhole profile was developed. The effects of plasma absorption through inverse Bremsstrahlung assuming different constant values of the related absorption coefficient were investigated, and different modelling strategies of multiple reflections of the beam rays were taken into account. It was demonstrated that an iterative ray-tracing technique, in which the effective distance of the path is precisely calculated for each ray of the laser beam, brings to a narrower and much deeper keyhole profile than the approximated averaged solution, where a mean number of reflections inside the keyhole are estimated with a simple formulation. In this work, the energy balance of the ray-tracing approach has been refined and extended to account for upward-oriented reflections, together with the plasma absorption via inverse Bremsstrahlung throughout the entire trajectory of each ray inside the keyhole. The inclusion of upward reflections, typically neglected in semi-analytical models, is crucial under certain conditions to accurately capture the physical energy balance of the process. While maintaining a fast and computationally efficient structure, the model enables a theoretical investigation into the physical mechanisms governing this specific phenomenon. In addition, the effects of the plasma plume damping over the keyhole are investigated performing different plume height conditions, for a CO₂-laser radiation. Then, the model is validated comparing the results with experimental tests, taken from the literature [22], considering two different welding configurations.

2. Model description

2.1. Semi-analytical model for the keyhole geometry

A semi-analytical approach for the investigation of the keyhole geometry was developed as a refinement of previous works [22,23] by including the local contribution of multiple reflections inside the keyhole plasma by means of a ray-tracing approach in which both upward- and downward-oriented reflections have been considered. As similar simplified approaches, this model neglected fluid dynamics, vapor-induced forces, surface tension effects, and metal vapor flow within the cavity, in order to be computational efficient. However, hybrid approaches coupling this model with more accurate and complete models (CFD, VOF) could be performed for a complete evaluation of all the phenomena involved. In this model, the keyhole profile is

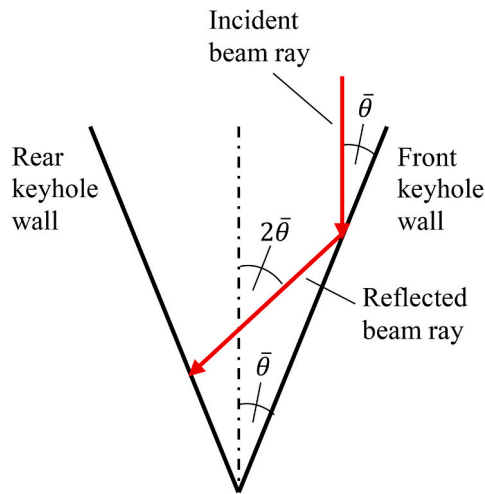


Fig. 3. Sketch of the simplified keyhole for the calculation of the multiple reflections, adapted from [23].

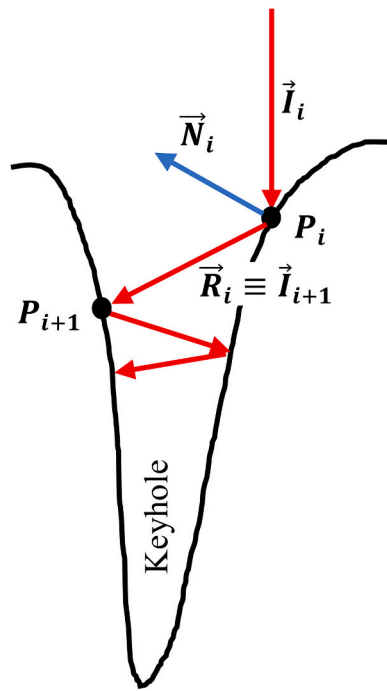


Fig. 4. Schematization of the multiple reflection calculation through a ray-tracing technique, adapted from [40].

calculated locally implementing the energy balance between the portion of laser power effectively absorbed and the flux dissipated by heat conduction in the workpiece, as represented in Fig. 1. The point-by-point calculation of the energy balance yields the local inclination of the front (advancing side) and the rear (retreating side) walls, therefore the geometry of the keyhole in the longitudinal section can be defined downward (Fig. 2). The model assumes an overall Cartesian coordinate system (x, y, z) , where the x axis is located along the welding direction, the z axis coincides with the beam axis, and the y axis is perpendicular to both. The origin of the coordinate system lies on the upper surface of the workpiece. In detail, the local keyhole wall angle θ could be determined, as a first simplified step, by the energy balance between the heat flux conducted into the keyhole wall, q_v , and the locally absorbed beam energy flux, I_a , according to the following relation:

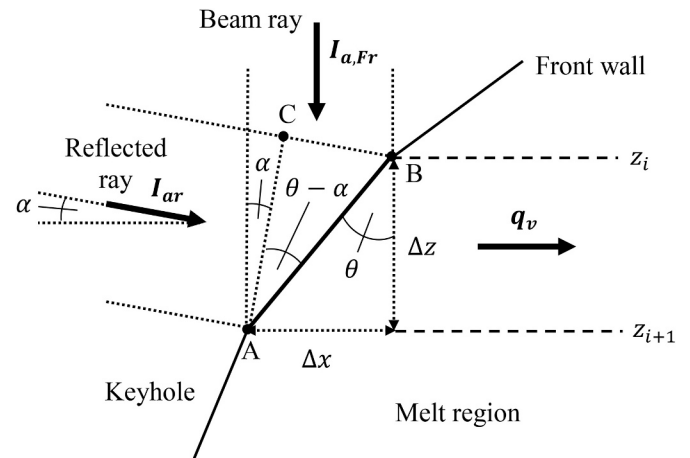


Fig. 5. Schematization of the energy balance with the energy contribution due to multiple reflections on a generic cell of the model.

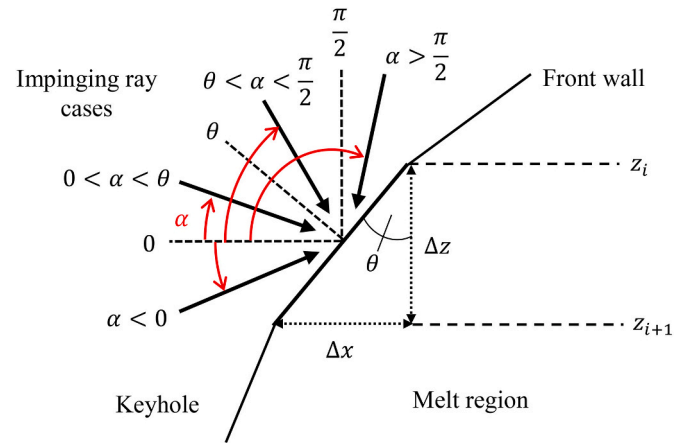


Fig. 6. Schematization of all the possible positions of an impinging ray on a generic cell of the model on the front keyhole wall.

$$\tan \theta = \frac{q_v}{I_a}. \quad (1)$$

Note that the Fig. 1 visualizes the main redistribution from almost vertical to almost horizontal heat flow. The accurate detailed temperature field starts as heat flux perpendicular to the surface, then bending to a widely horizontal heat flow. The illustration in Fig. 1 shows this transformation, while most of the keyhole wall angles will quantitatively be much steeper, almost vertical. Most important, the horizontal heat flux represents well the heat flow conditions in flat sheets, which are balanced by this local energy balance in the model.

The calculation of the wall heat flux should take into account the movement of the heat source relative to the workpiece. The moving line source model of Rosenthal [38] gives a solution for the two-dimensional temperature field in an infinite plate:

$$T(r, \varphi) = T_a + \frac{P'}{2\pi\lambda_{th}} K_0(Pe' r) e^{-Pe' r \cos \varphi}. \quad (2)$$

The solution refers to a location in the plate, in cylindrical coordinates (r, φ, z) , with the line source as the origin, and r, φ and z as the equivalent polar coordinates corresponding to x, y, z Cartesian coordinates. T_a is the ambient temperature, P' is the strength of the line source, i.e. power per unitary depth, λ_{th} denotes the thermal conductivity, K_0 is the second kind and zeroth-order solution of the modified Bessel function. Pe' is the modified Péclet number defined as follows:

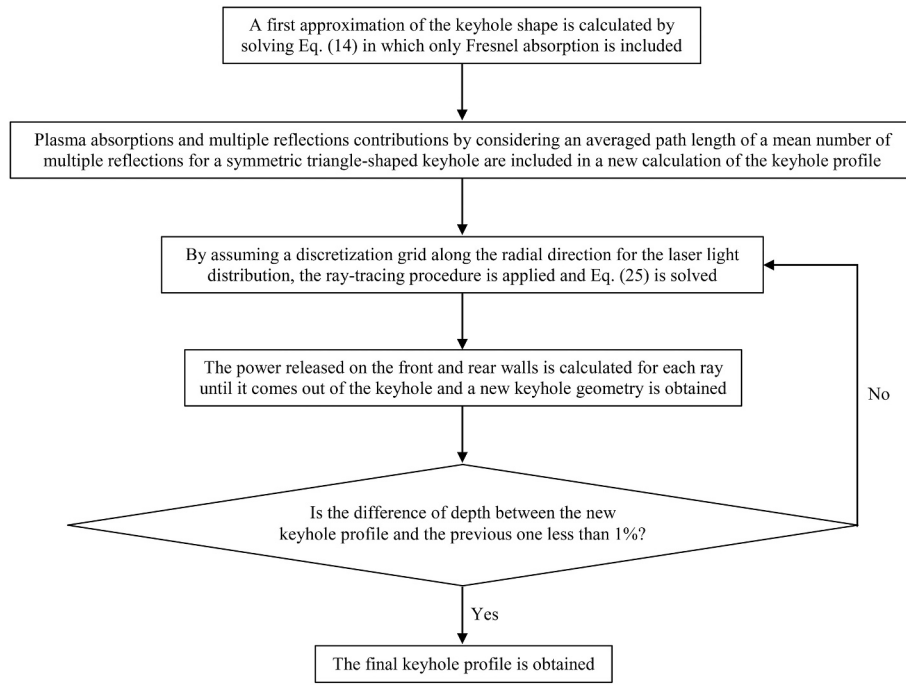


Fig. 7. Flow chart of the iterative numerical procedure for the calculation of the keyhole profile.

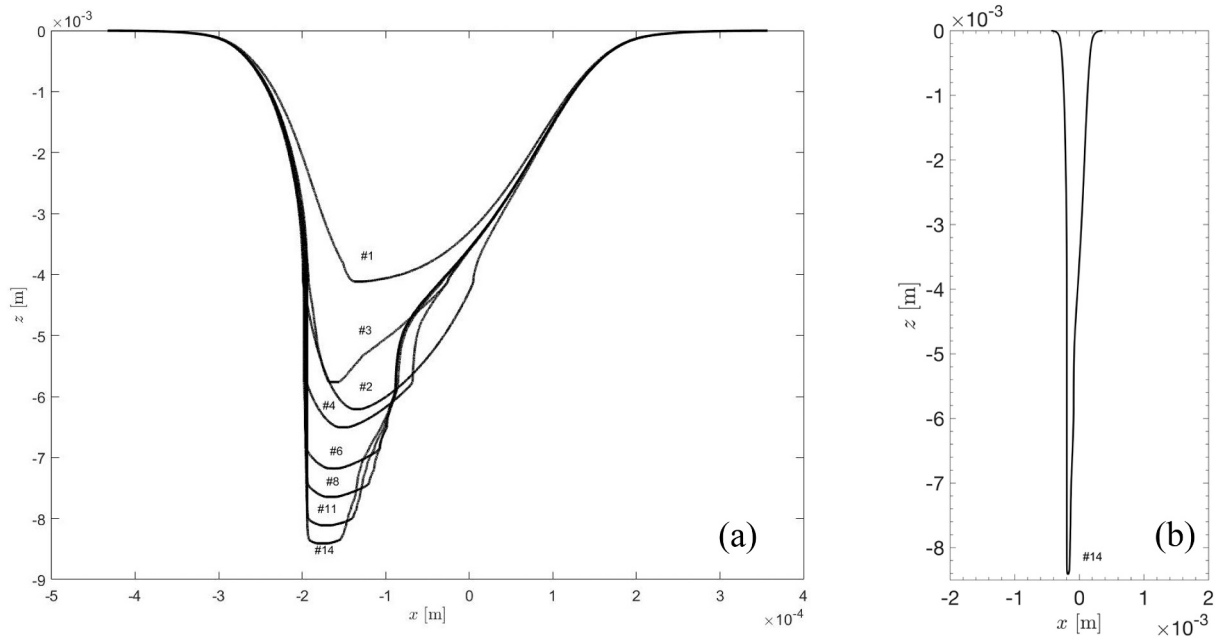


Fig. 8. (a) Sequence of keyhole profiles obtained with the iterative procedure ($P_L = 10$ kW and $v_w = 50$ mm/s). (b) Keyhole profile achieved in the last iteration with equal axis aspect ratio.

$$Pe' = v_w/2k, \quad (3)$$

that considers the welding speed v_w and the thermal diffusivity k .

The heat flow q_v inside the material may be derived with a mathematical procedure (already described in detail [22]) from the temperature field (Eq. (2)) by assuming that the temperature at the keyhole wall reaches the evaporation temperature T_v [22,23]:

$$q_v(r, \varphi) = (T_v - T_a)\lambda_{th}Pe' \left(\cos\varphi + \frac{K_1(Pe' r)}{K_0(Pe' r)} \right), \quad (4)$$

where K_1 is the modified Bessel function of the second kind and first

order. Eq. (4) is the main formula for the model used to describe the dissipated heat flux at each point of the keyhole wall. To obtain the keyhole profile in the longitudinal section ($x - z$ plane), Eq. (4) has to be considered in the two cases of interest of the azimuthal angles $\varphi = 0, \pi$:

$$q_v(x_{fs}, 0) = (T_v - T_a)\lambda_{th}Pe' \left(1 + \frac{K_1(Pe' x_{fs})}{K_0(Pe' x_{fs})} \right), \quad (5)$$

$$q_v(x_{rs}, \pi) = (T_v - T_a)\lambda_{th}Pe' \left(-1 + \frac{K_1(Pe' x_{rs})}{K_0(Pe' x_{rs})} \right). \quad (6)$$

Table 1

Process specifications and material properties considered for the calculation of the keyhole profiles.

Wavelength [μm]	10.6
Focal length [mm]	200
Focal radius [μm]	203
Beam diameter on optics [mm]	34
Focal plane position [mm]	−0.7
α_{iB} [m^{-1}]	100
ε_1	1
ε_2	1
σ_{st} [$\Omega^{-1} \text{m}^{-1}$]	$5 \cdot 10^5$
λ_{th} [$\text{Wm}^{-1} \text{K}^{-1}$]	$\lambda_{th}(T)$
T_v [K]	3273.15

Eqs. (5) and (6) describe the heat losses of any point at the keyhole front wall ($\varphi = 0$) and rear wall ($\varphi = \pi$) respectively, where x_{fs} and x_{rs} are the distances between the line source and the front and rear wall respectively (Fig. 2).

In addition, the local positions of the front and rear keyhole wall in the Cartesian coordinate system, respectively x_{fs} and x_{rs} , can be calculated by the following relation which can be derived from Eq. (2) [23]:

$$\frac{e^{Pe'x_{fs}}}{K_0(Pe'x_{fs})} = \frac{e^{-Pe'x_{rs}}}{K_0(Pe'x_{rs})}. \quad (7)$$

coupled with the following geometrical constraint

$$x_{fs} + x_{rs} = x_f - x_r. \quad (8)$$

In general, the front and rear walls have different local distances from the beam axis. It should be noticed that the beam axis (z axis) does not coincide with the moving line source, whose position x_s is defined by the following relations:

$$x_s = x_f - x_{fs} = x_r + x_{rs}. \quad (9)$$

The locally absorbed beam energy flux I_a in Eq. (1) is the fraction of the original laser beam intensity that actually enters the keyhole wall. The first step for the evaluation of I_a is to determine the intensity of the impinging beam ray I_l on the keyhole wall through a laser beam model with a Gaussian distribution.

The laser beam intensity I does not reach entirely the keyhole walls (i.e. $I_l < I$) due to several absorption mechanisms [22]. However, as a first approximation, all the plasma damping phenomena could be neglected (i.e. $I_l = I$), and the locally absorbed beam intensity at the keyhole wall should be calculated by considering at least the Fresnel absorption of the rays hitting the surface for the first time. In this case, the absorbed intensity I_a coincides with the laser intensity absorbed by Fresnel absorption mechanism $I_{a,Fr}$, which is obtained as follows:

$$I_{a,Fr} = \alpha_{Fr}(\chi)I_l, \quad (10)$$

where the Fresnel absorption coefficient α_{Fr} [39] is calculated as:

$$\alpha_{Fr}(\chi) = 1 - \frac{1}{2} \left(\frac{1 + (1 - \varepsilon \cos \chi)^2}{1 + (1 + \varepsilon \cos \chi)^2} + \frac{\cos^2 \chi + (\varepsilon - \cos \chi)^2}{\cos^2 \chi + (\varepsilon + \cos \chi)^2} \right). \quad (11)$$

This coefficient depends on the angle of reflection χ that the light makes with the normal of the hitting surface. Considering the local slope of the keyhole wall θ , the following relation is always verified for a vertical ray:

$$\chi = \frac{\pi}{2} - \theta. \quad (12)$$

In addition, α_{Fr} is related to the material-dependent quantity ε and is defined as

$$\varepsilon = \sqrt{\frac{2\varepsilon_2}{\varepsilon_1 + \sqrt{\varepsilon_1^2 + (\sigma_{st}/\omega\varepsilon_0)^2}}}, \quad (13)$$

where ε_0 is the permittivity of the vacuum, ε_1 and ε_2 are the real parts of the dielectric constants for the metal and the air or vapor through which the beam is transmitted, σ_{st} is the electrical conductivity per unit depth of the workpiece and ω is the frequency of the laser beam.

Therefore, considering the local energy balance (Eq.(1)) and discretizing the z axis, the slope of both the front and the rear keyhole walls can be calculated in the first instance as follows:

$$\frac{\Delta x}{\Delta z} = \tan \theta_i = \frac{q_v}{I_a} \cong \frac{q_v}{I_{a,Fr}}. \quad (14)$$

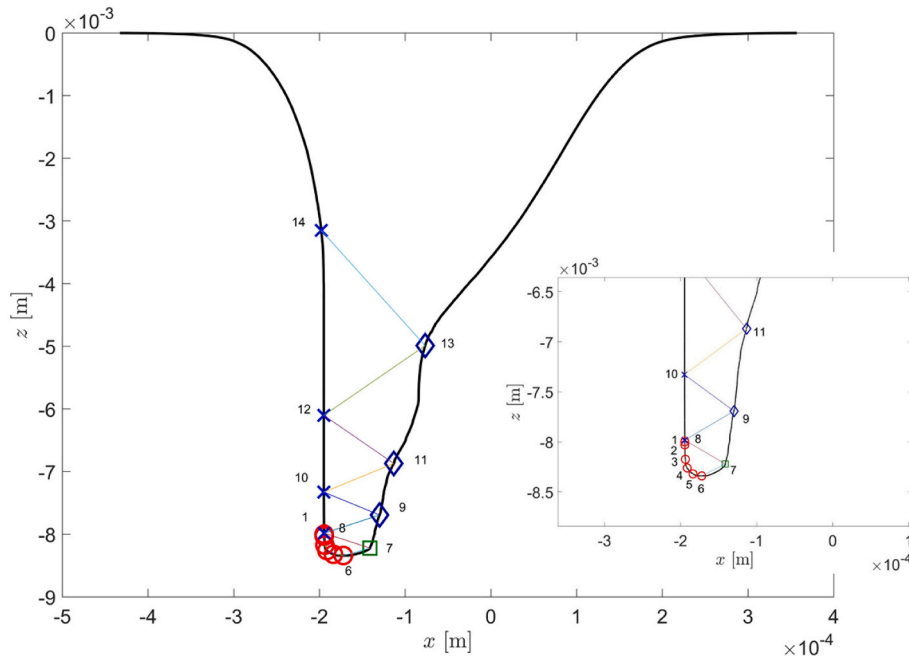


Fig. 9. Path evolution of a single ray emitted by the laser at $x = -1.95 \cdot 10^{-4}$ m as a function of the distance from the laser source. In the simulation $P_L = 10$ kW and $v_w = 50$ mm/s.

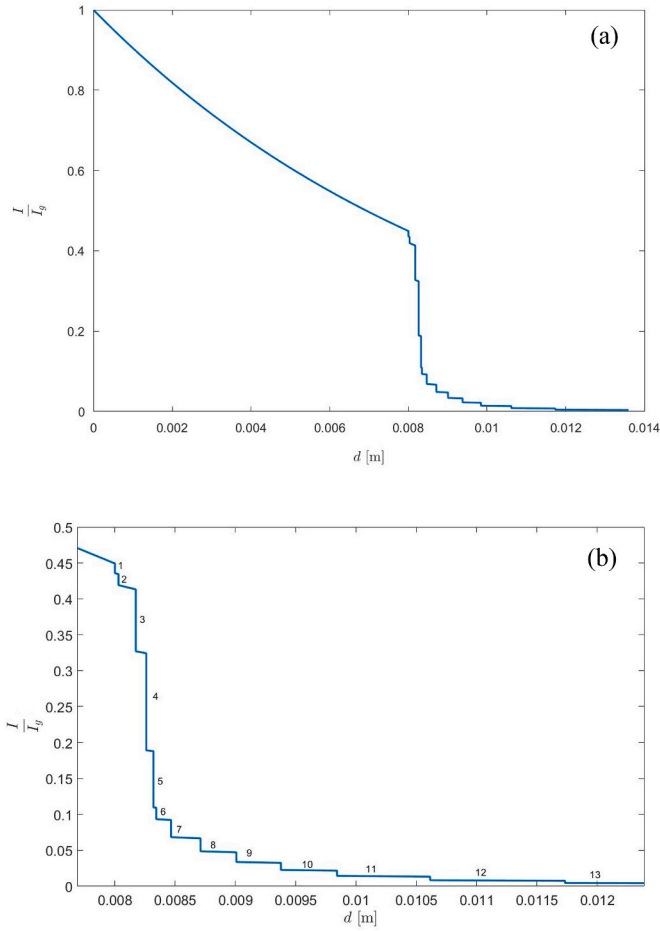


Fig. 10. Evolution of the normalized power density of a single ray starting at $x = -1.95 \cdot 10^{-4}$ m as a function of the distance d along the path. In the simulation, welding speed 50 mm/s and laser power 10 kW. (a) power evolution during the full path of the ray (b) power evolution of the ray inside the keyhole (magnification).

2.2. Plasma absorption and multiple reflections modelling

The keyhole profile calculated by considering only the Fresnel absorption should be refined with one or more additional runs that take into account all the plasma absorption mechanisms. Generally, the plasma absorption is considered as follows:

$$I_l = I_e^{-\alpha_{IB} l}, \quad (15)$$

where I_l is the power density directly irradiated by the laser, α_{IB} is the plasma absorption coefficient due to inverse Bremsstrahlung, and l represents the length of the path that the beam ray travels through the plasma inside the keyhole before hitting the wall surface. The length of the path l is usually estimated considering a mean path of the beam rays for each kind of absorption mechanism (plasma plume, first reflection, and successive multiple reflections absorptions). Generally, the applications of the asymmetric keyhole model take into account the plasma absorption through inverse Bremsstrahlung assuming a constant value of the related absorption coefficient, which is temperature-dependent. Moreover, the model considers also multiple reflection effects inside the keyhole. The earliest applications of the energy balance model simplify the calculation of this mechanism considering the keyhole profile as a symmetric triangle with a mean wall angle $\bar{\theta}$, as depicted in Fig. 3 [22,23].

Based on the optical geometry, the angle θ_r between the reflected

beam and the initial incident beam after n_{mr} reflections is calculated as

$$\theta_r = 2n_{mr}\bar{\theta}. \quad (16)$$

It is assumed that the reflected beam leaves the keyhole without being further absorbed when θ_r becomes higher than $\pi/2$. Therefore, the number of multiple reflections n_{mr} that the mean beam ray experiences inside the keyhole can be estimated as:

$$n_{mr} = \frac{\pi/2}{2\bar{\theta}} = \frac{\pi}{4\bar{\theta}} \quad (17)$$

More recent modifications of the same model treat multiple reflections with more robust ray-tracing or similar approaches, although considering only the downward orientated reflections [26,30]. The ray-tracing technique consists in discretizing the laser beam in a bundle of rays and calculating the exact path of each ray inside the keyhole through the following optical vector equation:

$$\vec{R}_i = \vec{T}_i + 2 \left(-\vec{T}_i \cdot \vec{N}_i \right) \vec{N}_i, \quad (18)$$

where \vec{R}_i is the vector of the reflected ray at the i -th reflection, \vec{T}_i the one of the incident ray, and \vec{N}_i indicates the surface normal at the irradiated point P_i , as schematized in Fig. 4 [40].

This calculation has to be reiterated for each i -th reflection of each ray inside the keyhole. Therefore, the accuracy of the calculation of the absorption contribution is related to the number of rays in which the laser beam is discretized: the higher is the number of beam rays considered, the more precise the calculation obtained, but also the higher the computational cost borne. The main novelty of the developed model is in the iterative calculation method based on the energy contribution by multiple reflections both in downward- and upward-directions and on the plasma attenuation along the entire path length of each ray, where l (Eq. 15) is precisely calculated for each beam ray and not estimated as an averaged value as usual. In more detail, as already introduced in a previous work [37], a ray-tracing approach has been adopted in which the energy deposited in each point by the reflected rays is stored and the emerging ray power is updated. Then, the energy balance is solved again in successive iterative steps including the contribution of the additional energy due to multiple reflections inside the keyhole, as depicted in Fig. 5. This contribution is assumed as additional rays with their own power density that irradiate each portion of the surface on the front and the rear keyhole walls.

The effective power density of the i -th reflected ray I_{ar_i} , which contributes to the overall energy balance, takes into account the Fresnel absorption net of the plasma damping phenomena before hitting the keyhole wall:

$$I_{ar_i} = \alpha_{Fr}(\varphi) I_{r_i}, \quad (19)$$

where the term I_{r_i} is obtained considering the Fresnel reflected part of the i -th ray just as I_l (Eq. (15)). Therefore, the following equation,

$$I_{a,Fr} \Delta x + I_{ar} \frac{\Delta x \cos(\theta - \alpha)}{\sin(\theta)} = q_v \Delta z, \quad (20)$$

can be obtained, with reference to the notation of Fig. 5, considering that:

$$\overline{AC} = \overline{AB} \cos(\theta - \alpha), \quad (21)$$

$$\overline{AB} = \frac{\Delta x}{\sin(\theta)}, \quad (22)$$

$$\overline{AC} = \frac{\Delta x \cos(\theta - \alpha)}{\sin(\theta)}. \quad (23)$$

Eq. (20) can be reformulated as follows:

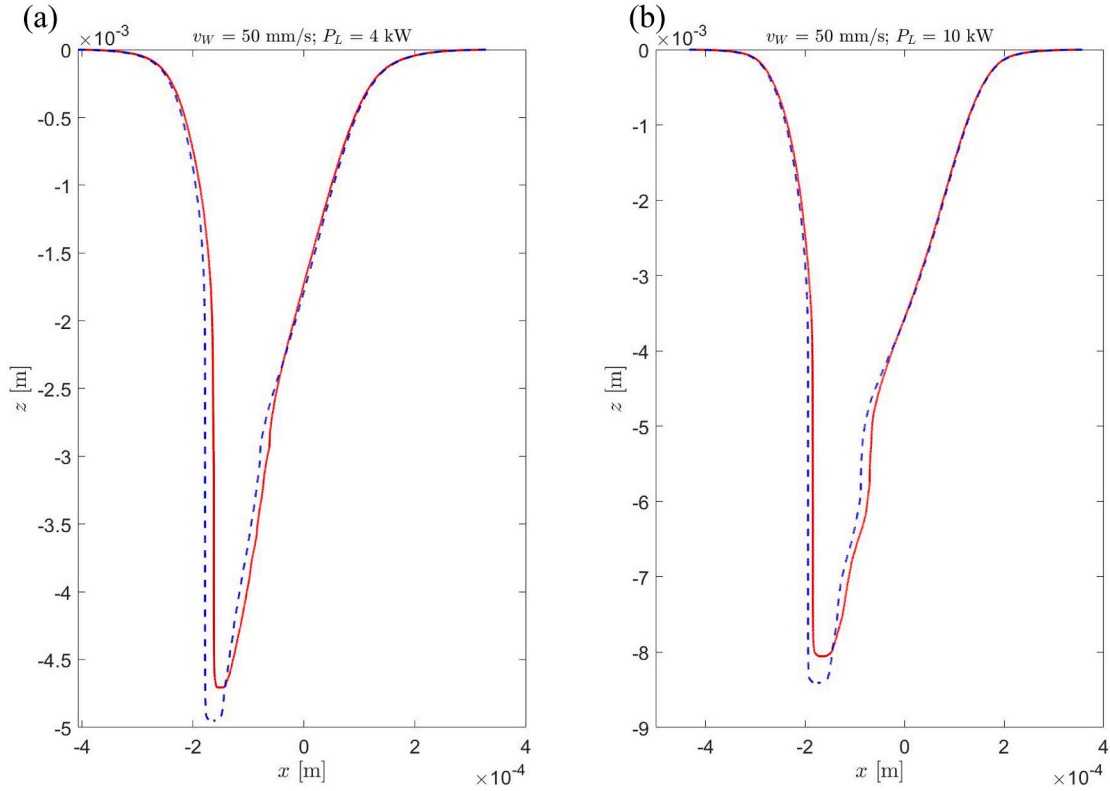


Fig. 11. Keyhole profiles obtained imposing welding speed 50 mm/s and laser power 4 kW (a) and 10 kW (b), with (dashed blue curves) and without (red curves) considering the energy contribution from upward-oriented rays. (For interpretation of the references to colour in this figure legend, the reader is referred to the web version of this article.)

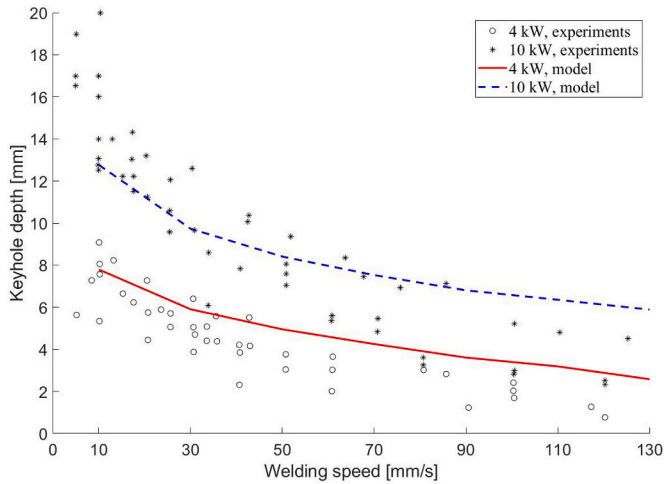


Fig. 12. Keyhole profile depths obtained considering two levels of laser power (4 and 10 kW) in the range of welding speed from 10 to 130 mm/s compared with experimental results showed by Kaplan [22].

$$\frac{\Delta x}{\Delta z} = \tan\theta = \frac{q_v}{I_{a,Fr} + I_{ar} \frac{\cos(\theta-\alpha)}{\sin(\theta)}} \quad (24)$$

that recalls the formulation of the local energy balance (Eq.(1)). Considering all the N reflected rays, each with its inclination angle α_i , hitting the same portion of wall surface, the new energy balance for that portion can be finally written as

$$\tan\theta = \frac{q_v}{I_{a,Fr} + \sum_{i=1}^N I_{ar_i} \frac{\cos(\theta-\alpha_i)}{\sin(\theta)}} \quad (25)$$

Eq. (25) is valid for all the possible positions of the impinging ray, included upward-oriented rays ($\alpha < 0$) that are commonly neglected. Fig. 6 shows an example on a generic cell of the front keyhole wall, but it continues to be true, for symmetry, on the rear wall.

The numerical procedure for the calculation of the keyhole geometry follows the steps summarized in the flowchart depicted in Fig. 7 and, in particular:

- a) an initial keyhole profile is calculated by considering the average contribution of the multiple reflections as given in [20]. The procedure consists of two steps: the calculation of the profile of the keyhole by including only Fresnel absorption; a subsequent evaluation of the profile in which an averaged path length of a mean number of multiple reflections for a symmetric triangle-shaped keyhole are included. The depth of the triangle-shaped keyhole has been evaluated as a result of the first step;
- b) the laser source represented by the incident Gaussian intensity distribution of the light is decomposed into individual rays and the path of each ray is traced out during multiple reflections both in downward- and upward- directions until the ray comes out of the keyhole. The power released on each grid point of the front and rear walls is calculated for each ray;
- c) a new keyhole profile is calculated by means of the energy balance of Eq. (25) in which power stored in b) is included point by point;
- d) steps b and c are repeated until the difference of depth between the new keyhole profile and the previous one is $< 1\%$

In particular, the error threshold of 1 % was chosen in order to obtain the keyhole profile performing < 20 iterations. This allowed an accurate

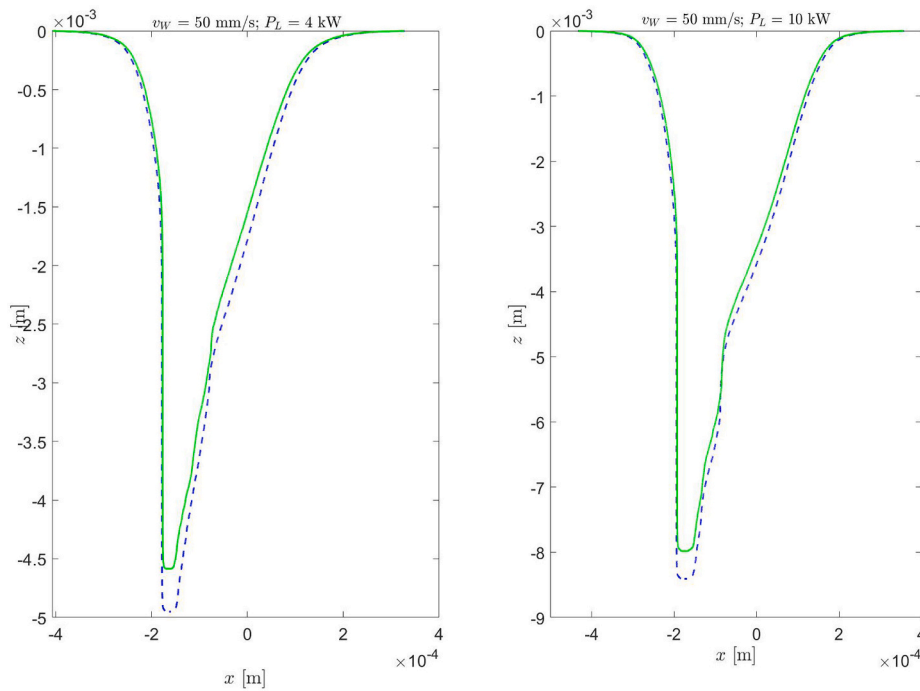


Fig. 13. Keyhole profiles obtained imposing welding speed 50 mm/s and laser power 4 kW (a) and 10 kW (b), considering the energy contribution from upward-oriented rays without (dashed blue curves) and with (green curves) taking into account the absorption effects of 1.2 mm-high plasma plume. (For interpretation of the references to colour in this figure legend, the reader is referred to the web version of this article.)

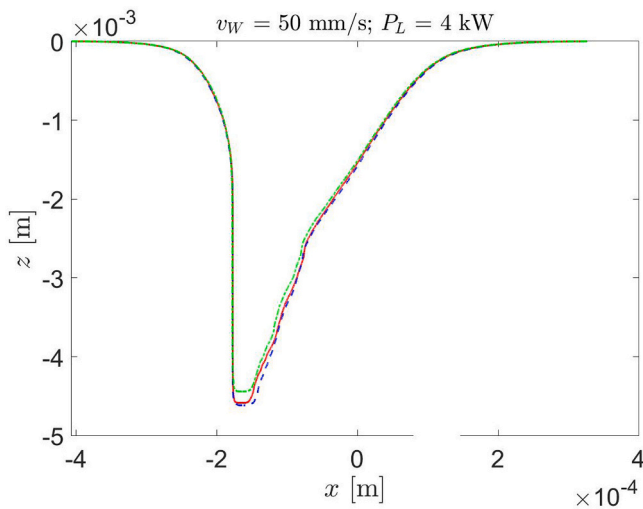


Fig. 14. Keyhole profiles obtained imposing welding speed 50 mm/s, laser power 4 kW, and mean plasma plume height of 1 mm (blue dashed curve), 1.2 mm (red curve), and 1.4 mm (green dot-dashed curve). (For interpretation of the references to colour in this figure legend, the reader is referred to the web version of this article.)

stationary solution and a stable final profile despite all the assumptions and limitations of the model. Number of iterations is anyway strictly dependent on the initial guess given in step a). As an example, keyhole profiles have been depicted in Fig. 8a in which the sequence of keyhole profiles obtained following the procedure described in a)-d) is represented. The final keyhole profile has been obtained after 14 iterations in the case of $P_L = 10$ kW and $v_W = 50$ mm/s, laser welding process parameters listed in Table 1 and thermophysical properties of the material (low alloyed steel) taken from the literature [41]. Note the different scales applied in the graphs for the x - and z -axis, for better visualization

of the conditions, which displays different aspect ratios and angles. The keyhole profile achieved in the last iteration with the actual aspect ratio (same scale for x and z) is reported in Fig. 8b. The here presented approach is an efficient method to study specific mechanisms, like absorption, multiple reflections and the keyhole shape, in the xz -plane. Among the simplifications can be mentioned the neglect of melt and vapor flow, of the three-dimensional keyhole shape and accordingly 3D-multiple reflections, time dependent fluctuations and temperature-dependent material properties. Despite simplifications, the results are assessed to be sufficiently representative for process trends and orders of magnitude estimations.

3. Results and discussion

Numerical simulations have been performed in the case of laser welding of steel [32] for different operating (power of the laser, welding speed) and process parameters, as listed in Table 1. CO₂-laser beam welding is studied, which can cause significant plasma absorption in metal vapor.

As an example, Figs. 9 and 10 show the evolution of the path and of the normalized power of a single ray starting at $x = -1.95 \cdot 10^{-4}$ m as a function of the distance from the laser source. The path of the ray emitted by the laser is characterized by 14 interactions with the rear and the front sides of the keyhole before leaving the keyhole. Fig. 10 shows the normalized evolution of the power during the path of the selected ray. Numerical results obtained with the iterative procedure show that the most significant energy damping is related to the first travel of the laser ray through the keyhole plasma before hitting the keyhole wall for the first time in its lowest region. Regarding the contribution of the downward (1–6) and upward (7–14) directions, 10 % of the power is related to the upward contribution, highlighting its not totally negligible role.

In Fig. 9, the selected ray shows how the upper part of the keyhole front might be mainly governed by direct incidence of the laser beam while in the lower region significant energy is added from multiple reflections, altering the main controlling mechanism of the angle. In this

keyhole shape, several reflections occur very close to each other at the bottom. To some extent the model is sensitive to alterations of the local keyhole shape and wall angle, which can be studied by more complex and time-dependent calculations. However, the main trends predicted by the model can be regarded as representative, acquired by a very efficient model. Similarly, any other ray of the laser beam can be traced and analysed, also for statistical evaluation.

After significant plasma absorption, the first five interactions of the ray with the keyhole surface led to significant absorption, as displayed in Fig. 10, thanks to the favourable angle range for the Fresnel absorption. Note that the keyhole in Fig. 9 is magnified in horizontal direction, so the angles of incidence are much steeper than they appear.

In Fig. 10 the normalized power density is represented as a function of the effective flight distance travelled by the ray before coming out the keyhole at the end of upward reflections, which is higher (14 mm) than the depth of the keyhole (8.5 mm). Only about 10 % of the power in the studied ray was left, for the remaining reflections. This is valid for the selected ray. As will be shown below, this is different for other rays of the beam, since the overall calculation has yielded a significant absorption contribution by the late back reflections. This example demonstrates how the semi-analytical model can efficiently provide valuable, relevant estimations of a very complex interaction mechanism.

Fig. 11 shows the keyhole profiles calculated for two laser power (P_L) values, with and without considering the upward reflections. A smooth change in the slope is observed along the keyhole profile for both the P_L levels. The front and rear walls become steeper at approximately half the total depth of the keyhole. As already stated in the literature [22,37], while the difference of slope between front and rear keyhole is due to the convective effects of the welding speed, the steepness of the keyhole walls is directly related to the heat conduction phenomenon inside the workpiece. Therefore, the increased slope of the lowest parts of both the keyhole walls is due to the increase of the reflected energy inside the keyhole since also upward reflections are taken into account and these ones are gathered above all in the deepest part of the keyhole. The results show that the calculation including also the upward-oriented rays results in deeper and slightly narrower keyhole geometries than the model which completely neglects them. Differences of 4.9 % (from 4.70 to 4.95 mm) and 4.2 % (from 8.06 to 8.41 mm) were registered in the keyhole depth considering welding configurations with $P_L = 4$ kW (Fig. 11a) and $P_L = 10$ kW (Fig. 11b) respectively, both with $v_w = 50$ mm/s. Partial penetration was studied, i.e. sheets thicker than the resulting keyhole depth. These results confirm that the upward-oriented rays give a sizeable energy contribution that should be considered for finer modelling of the keyhole geometry.

The keyhole depth values obtained from the refined model considering two levels of laser power (4 and 10 kW) and several welding speeds (from 10 to 130 mm/s) are represented in Fig. 12. These results follow the same trend of the experimental tests conducted in the investigated welding conditions and reported in the literature [22]. In addition, the keyhole depth values obtained numerically show good accordance with the experimental ones for lower and medium welding speeds. It is important to notice that Kaplan [22], which used a similar semi-analytical model but considering multiple reflections with averaged geometrical approximation, observed deeper penetrations than experimental values at lower velocities. This confirms that the refined model used in this work is more reliable in the prediction of keyhole geometries for lower welding speeds. On the other hand, the model developed tends to overestimate the keyhole depths for higher velocities, above all in the lower laser power configuration. A possible reason for these discrepancies could be found in the modelling of the plasma absorption mechanism due to inverse Bremsstrahlung through a constant mean value of the related coefficient $\alpha_{IB} = 100 \text{ m}^{-1}$ [22]. As already stated in a previous work [37], α_{IB} is directly related to the plasma temperature, and the variation of its value could bring noticeable differences in the keyhole depth. Therefore, the constant value of $\alpha_{IB} = 100 \text{ m}^{-1}$ imposed in this study could result unfitting for the welding configurations

characterized by lower heat input, i.e. lower laser power and/or higher welding speed. The results obtained in a previous work [37] showed that the keyhole depth decreases with an increase of the α_{IB} value. This suggests that the plasma absorption effects due to inverse Bremsstrahlung could be underestimated by the model when the heat input lowers. For more accurate evaluations, the α_{IB} value should be calculated considering its dependence on the plasma temperature and electron densities [37]. This approach goes beyond the scope of this work and will be developed in future publications.

Another factor that affects the keyhole penetration is the damping effect in the plasma plume, which was neglected in the first set of calculations. The absorption effects of plasma plume with an imposed mean height of 1.2 mm [22] on the keyhole geometry were evaluated considering again the configurations with fixed $v_w = 50$ mm/s and with $P_L = 4$ kW and $P_L = 10$ kW (Fig. 13). The plasma plume damping entails a decrease of the keyhole depth of 7.4 % (from 4.95 to 4.59 mm) in the lowest laser power case, and 5.1 % (from 8.41 to 7.98 mm) in the highest laser power case. In both cases, only slightly narrower keyhole profiles without substantial reshaping were observed considering the plasma plume absorption.

Generally, the laser welding process is carried out using shielding inert gases (e.g. Ar or He) which contributes, in addition to protect the molten pool against oxidation, to reduce the plasma plume height, and so its absorption effects on the laser beam. Therefore, plasma plume damping could differ also varying the shielding gas flow rate, velocity, and direction, which have an impact on the plasma plume height that the laser beam passes through. Fig. 14 compares the keyhole geometries obtained considering three different mean plasma plume heights. An increase of the mean plume height of 0.2 mm from the starting configuration (i.e. plume height of 1.4 mm) implies higher plasma plume damping effects, with a keyhole depth reduction of 3.3 % (from 4.59 to 4.44 mm). Instead, a mean plume height of 1.0 mm (i.e. 0.2 mm lower than the starting configuration, which entails lower laser beam attenuation) causes an increase of 0.6 % of the keyhole cavity depth (from 4.59 to 4.62 mm). Also in this case, more accurate investigations on the effects of the shielding gas flow conditions on the plasma plume height should be done, going beyond the purpose of this study, which is mainly focused on the contribution of upward-directed rays in multiple reflection mechanism. Finally, it should be noticed that, in some conditions, an experimental error up to 15 % can be observed. Although this difference could result greater than the differences on the keyhole geometry obtained with the aforementioned model refinements, the improvements presented in this study allow to highlight those specific physical effects related to the laser-plasma interaction rather than dramatically enhance prediction in any case study. Plasma effects (bulk or plume contributions) and multiple reflections, including upward oriented ones, could, for instance, become significant in some conditions (i.e. shallow profiles, or particular composition of plasma shielding gas or bulk plasma characterized by a particular composition of the metals to be welded).

4. Conclusions

The described model allows to calculate the keyhole profile during laser-matter interaction solving the local energy balance in which all the reflected rays that hit the keyhole walls have been considered together with the plasma absorption through inverse Bremsstrahlung during their travel inside the keyhole. The power released is absorbed by the walls transferring energy to the molten material, including the upward-oriented ones which are commonly neglected in similar approaches. The following conclusions can be drawn.

- The observation of selected ray paths within the plasma keyhole demonstrates that the upper part of the keyhole front is predominantly governed by the direct incidence of the laser beam; in contrast, the lower region receives a substantial portion of energy

through multiple reflections, which decisively shift the dominant mechanism controlling the keyhole's inclination angle.

- The upward-oriented reflected rays give a noticeable contribution to the local energy balance. The comparisons made in this study considering two different laser welding configurations ($v_w = 50$ mm/s and $P_L = 4$ kW; $v_w = 50$ mm/s and $P_L = 10$ kW) showed that the keyhole depth increases of 4.9 % (from 4.70 to 4.95 mm) in the first configuration and 4.2 % (from 8.06 to 8.41 mm) in the second configuration taking into account the upward reflected rays. Also, the keyhole shape varied considering these additional rays with a slight shift backward with respect to the laser travelling direction. In both configurations, the keyhole walls were steeper in the lowest part since the upward reflected rays gather in the deepest part of the keyhole. This confirmed that the energy losses due to the reflection of rays exiting the keyhole occur mainly from the upper regions of the keyhole.
- The model that takes into account also upward-oriented reflected rays was experimentally validated considering welding configurations with two levels of laser power ($P_L = 4$ kW and $P_L = 10$ kW) and a wide range of welding speeds ($v_w = 10 \div 130$ mm/s). The numerical-experimental comparison revealed that the described model is able to properly predict the keyhole depth values especially for lower and medium welding speeds with a slight overestimation of the depth for higher values of the welding speed
- Also the damping effect in the plasma plume above the keyhole has a considerable role in the energy balance and the keyhole geometry. The insertion in the model of 1.2 mm-high plasma plume caused a reduction of the keyhole depth of 7.4 % (from 4.95 to 4.59 mm) considering the welding configuration with $v_w = 50$ mm/s and $P_L = 4$ kW, and 5.1 % (from 8.41 to 7.98 mm) considering the welding configuration with $v_w = 50$ mm/s and $P_L = 10$ kW, with respect to the model that completely neglects the plasma plume damping. However, no significant keyhole shape variations were registered. Finally, the effects related to an increase and a decrease of 0.2 mm of the mean plasma plume height from the starting value of 1.2 mm were investigated. The lower plume height of 1.0 mm led to a reduction of damping effects causing an increase of 0.6 % of the keyhole cavity depth (from 4.59 to 4.62 mm). On the other hand, the 1.4 mm-high plasma plume brought to 3.3 % shallower keyhole (from 4.59 to 4.44 mm) due to a greater laser beam absorption.

Future works will be aimed at applying the model to different laser wavelengths and power density distributions and at solving some of its limitations. For instance, the implementation of a refined contribution of the plasma inside the keyhole in which the plasma shall be treated as a collection of charged particles with changing transport and thermodynamic properties with the pressure and temperature. Furthermore, fluid dynamic effects, such as metal vapor flow and surface tension forces could be added to the model. Another potential development is the integration of the model in a hybrid approach, coupling it with more accurate and complete models (CFD, VOF) in order to evaluate the effects of multiple reflections by means of sufficiently accurate and not pre-assumed hole shapes.

CRedit authorship contribution statement

Donato Coviello: Writing – review & editing, Writing – original draft, Validation, Software, Methodology, Investigation, Formal analysis, Data curation, Conceptualization. **Antonio D'Angola:** Writing – review & editing, Supervision, Software, Methodology, Investigation, Formal analysis, Data curation, Conceptualization. **Donato Sorgente:** Writing – review & editing, Supervision, Resources, Methodology, Investigation, Conceptualization. **Alexander F.H. Kaplan:** Writing – review & editing, Validation, Supervision.

Declaration of competing interest

The authors declare that they have no known competing financial interests or personal relationships that could have appeared to influence the work reported in this paper.

References

- [1] Shcheglov P. Study of vapour-plasma plume during high power fiber laser beam influence on metals. 2012.
- [2] Rai R, Elmer JW, Palmer TA, Debroy T. Heat transfer and fluid flow during keyhole mode laser welding of tantalum, Ti-6Al-4V, 304L stainless steel and vanadium. *J Phys D Appl Phys* 2007;40:5753–66. <https://doi.org/10.1088/0022-3727/40/18/037>.
- [3] Svenungsson J, Choquet I, Kaplan AFH. Laser welding process – a review of keyhole welding modelling. *Phys Procedia* 2015;78:182–91. <https://doi.org/10.1016/j.phpro.2015.11.042>.
- [4] Wang HX, Chen X. Three-dimensional modelling of the laser-induced plasma plume characteristics in laser welding. *J Phys D Appl Phys* 2003;36:628–39. <https://doi.org/10.1088/0022-3727/36/6/304>.
- [5] Chen X, Wang HX. Prediction of the laser-induced plasma characteristics in laser welding: a new modelling approach including a simplified keyhole model. *J Phys D Appl Phys* 2003;36:1634–43. <https://doi.org/10.1088/0022-3727/36/13/332>.
- [6] Graf T, Berger P, Weber R, Hügel H, Heider A, Stritt P. Analytical expressions for the threshold of deep-penetration laser welding. *Laser Phys Lett* 2015;12:56002. <https://doi.org/10.1088/1612-2011/12/5/056002>.
- [7] Semak VV, Bragg WD, Damkroger B, Kempka S. Transient model for the keyhole during laser welding. *J Phys D Appl Phys* 1999;32. <https://doi.org/10.1088/0022-3727/32/15/103>.
- [8] Ki H, Mohanty PS, Mazumder J. Modeling of laser keyhole welding: part II. Simulation of keyhole evolution, velocity, temperature profile, and experimental verification. *Metall Mater Trans A Phys Metall Mater Sci* 2002;33A:1831. [10.1007/s11661-002-0191-5.pdf](https://doi.org/10.1007/s11661-002-0191-5.pdf).
- [9] Fabbro R. Melt pool and keyhole behaviour analysis for deep penetration laser welding. *J Phys D Appl Phys* 2010;43. <https://doi.org/10.1088/0022-3727/43/44/445501>.
- [10] Tan W, Bailey NS, Shin YC. Investigation of keyhole plume and molten pool based on a three-dimensional dynamic model with sharp interface formulation. *J Phys D Appl Phys* 2013;46. <https://doi.org/10.1088/0022-3727/46/5/055501>.
- [11] Matsunawa A, Kim J-D, Seto N, Mizutani M, Katayama S. Dynamics of keyhole and molten pool in laser welding. *J Laser Appl* 1998;10:247–54. <https://doi.org/10.2351/1.521858>.
- [12] Seto N, Katayama S, Matsunawa A. High-speed simultaneous observation of plasma and keyhole behavior during high power CO2 laser welding: effect of shielding gas on porosity formation. *J Laser Appl* 2000;12:245–50. <https://doi.org/10.2351/1.1324717>.
- [13] Kaplan AFH, Mizutani SK Masami, Matsunawa A. Unbounded keyhole collapse and bubble formation during pulsed laser interaction with liquid zinc. *J Phys D Appl Phys* 2002;35:1218–28. <https://doi.org/10.1088/0022-3727/35/11/319>.
- [14] Kawahito Y, Mizutani M, Katayama S. Elucidation of high-power fibre laser welding phenomena of stainless steel and effect of factors on weld geometry. *J Phys D Appl Phys* 2007;40:5854–9. <https://doi.org/10.1088/0022-3727/40/19/009>.
- [15] Kawahito Y, Matsumoto N, Abe Y, Katayama S. Relationship of laser absorption to keyhole behavior in high power fiber laser welding of stainless steel and aluminum alloy. *J Mater Process Technol* 2011;211:1563–8. <https://doi.org/10.1016/j.jmatprotec.2011.04.002>.
- [16] Pang S, Chen X, Zhou J, Shao X, Wang C. 3D transient multiphase model for keyhole, vapor plume, and weld pool dynamics in laser welding including the ambient pressure effect. *Opt Lasers Eng* 2015;74:47–58. <https://doi.org/10.1016/j.optlaseng.2015.05.003>.
- [17] Cho JH, Na SJ. Three-dimensional analysis of molten pool in GMA-laser hybrid welding. *Weld J Miami Fla* 2009;88:35–44.
- [18] Ki H, Mohanty PS, Mazumder J. Modelling of high-density laser-material interaction using fast level set method. *J Phys D Appl Phys* 2001;34:364–72. <https://doi.org/10.1088/0022-3727/34/3/320>.
- [19] Courtois M, Carin M, Le Masson P, Gaied S, Balabane M. A new approach to compute multi-reflections of laser beam in a keyhole for heat transfer and fluid flow modelling in laser welding. *J Phys D Appl Phys* 2013;46:505305. <https://doi.org/10.1088/0022-3727/46/5/505305>.
- [20] Meena A, Lassila AA, Lonn D, Salomonsson K, Wang W, Nielsen CV, et al. Numerical and experimental study of the variation of keyhole depth with an aluminum alloy (AA1050). *J Adv Join Process* 2024;9:100196. <https://doi.org/10.1016/j.jajp.2024.100196>.
- [21] Zhu B, Zou J, Xie S, Liu T, Yang W. The calculation of keyhole depth based on the primary absorption of front keyhole wall in laser deep-penetration welding. *J Appl Phys* 2025;137. <https://doi.org/10.1063/5.0233981>.
- [22] Kaplan A. A model of deep penetration laser welding based on calculation of the keyhole profile. *J Phys D Appl Phys* 1994;27:1805–14. <https://doi.org/10.1088/0022-3727/27/9/002>.
- [23] Zhao H, DeRoy T. Macroporosity free aluminum alloy weldments through numerical simulation of keyhole mode laser welding. *J Appl Phys* 2003;93:10089–96. <https://doi.org/10.1063/1.1573732>.

- [24] Rai R, Debroy T. Tailoring weld geometry during keyhole mode laser welding using a genetic algorithm and a heat transfer model. *J Phys D Appl Phys* 2006;39: 1257–66. <https://doi.org/10.1088/0022-3727/39/6/037>.
- [25] Rai R, Kelly SM, Martukanitz RP, DebRoy T. A convective heat-transfer model for partial and full penetration keyhole mode laser welding of a structural steel. *Metall Mater Trans A Phys Metall Mater Sci* 2008;39:98–112. <https://doi.org/10.1007/s11661-007-9400-6>.
- [26] Xu GX, Wu CS, Qin GL, Wang XY, Lin SY. Adaptive volumetric heat source models for laser beam and laser + pulsed GMAW hybrid welding processes. *Int J Adv Manuf Technol* 2011;57:245–55. <https://doi.org/10.1007/s00170-011-3274-x>.
- [27] Kaplan AFH. Influence of the beam profile formulation when modeling fiber-guided laser welding. *J Laser Appl* 2011;23:042005. <https://doi.org/10.2351/1.3633221>.
- [28] Kaplan AFH. Fresnel absorption of 1 μm - and 10 μm -laser beams at the keyhole wall during laser beam welding: comparison between smooth and wavy surfaces. *Appl Surf Sci* 2012;258:3354–63. <https://doi.org/10.1016/j.apsusc.2011.08.086>.
- [29] Chowdhury S, Nirsanametla Y, Manapuram M. Investigation on keyhole mode fiber laser welding of SS 316 in a self-protected atmosphere. *Proc Inst Mech Eng Part C J Mech Eng Sci* 2019;233:6602–15. <https://doi.org/10.1177/0954406219864137>.
- [30] Jahn M, Montalvo-Urquiza J. Modeling and simulation of keyhole-based welding as multi-domain problem using the extended finite element method. *Appl Math Model* 2020;82:731–47. <https://doi.org/10.1016/j.apm.2020.01.072>.
- [31] Han SW, Ahn J, Na SJ. A study on ray tracing method for CFD simulations of laser keyhole welding: progressive search method. *Weld World* 2016;60:247–58. <https://doi.org/10.1007/s40194-015-0289-1>.
- [32] Pang S, Chen W, Zhou J, Liao D. Self-consistent modeling of keyhole and weld pool dynamics in tandem dual beam laser welding of aluminum alloy. *J Mater Process Technol* 2015;217:131–43. <https://doi.org/10.1016/j.jmatprotec.2014.11.013>.
- [33] Meng X, Putra SN, Bachmann M, Artinov A, Rethmeier M. Influence of the free surface reconstruction on the spatial laser energy distribution in high power laser beam welding modeling. *J Laser Appl* 2022;34. <https://doi.org/10.2351/7.0000739>.
- [34] Ki H, Mohanty PS, Mazumder J. Multiple reflection and its influence on keyhole evolution. *J Laser Appl* 2002;14:39–45. <https://doi.org/10.2351/1.1449885>.
- [35] Allen TR, Huang W, Tanner JR, Tan W, Fraser JM, Simonds BJ. Energy-coupling mechanisms revealed through simultaneous keyhole depth and Absorptance measurements during laser-metal processing. *Phys Rev Appl* 2020;13:1. <https://doi.org/10.1103/PHYSREVAPPLIED.13.064070>.
- [36] Huang W, Deisenroth D, Mekhontsev S, Tan W. Correlation between keyhole geometry and reflected laser light distribution in laser-based manufacturing. *Manuf Lett* 2023;38:56–9. <https://doi.org/10.1016/j.mfglet.2023.09.002>.
- [37] Coviello D, D'Angola A, Sorgente D. Numerical study on the influence of the plasma properties on the keyhole geometry in laser beam welding. *Front Phys* 2022;9:1–9. <https://doi.org/10.3389/fphy.2021.754672>.
- [38] Rosenthal, D. The theory of moving sources of heat and its application to metal treatments, in: *trans ASME*, 68, 8, n.d.: 849–866.
- [39] Dowden JM. The mathematics of thermal modeling. *An introduction to the theory of laser material processing*. CHAPMAN & HALL/CRC; 2001.
- [40] Cho J-H, Na S-J. Implementation of real-time multiple reflection and Fresnel absorption of laser beam in keyhole. *J Phys D Appl Phys* 2006;39:5372–8. <https://doi.org/10.1088/0022-3727/39/24/039>.
- [41] Kaars J, Mayr P, Koppe K. Determining material data for welding simulation of presshardened steel. *Metals (Basel)* 2018;8. <https://doi.org/10.3390/met8100740>.